Evolution of Electromagnetic Signatures of Sea Ice from Initial Formation to the Establishment of Thick First-Year Ice

Thomas C. Grenfell, *Associate Member, IEEE*, David G. Barber, A. K. Fung, *Fellow, IEEE*, Anthony J. Gow, Kenneth C. Jezek, *Associate Member, IEEE*, E. J. Knapp, Son V. Nghiem, *Member, IEEE*, Robert G. Onstott, *Member, IEEE*, Donald K. Perovich, Collin S. Roesler, C. T. Swift, *Fellow, IEEE*, and F. Tanis

***Abstract*— The spatial and temporal distribution of new and young sea ice types are of particular interest because of the influence this can exert on the heat and mass balance of the polar sea ice. The objective of the present work is to characterize the temporal evolution of the electromagnetic (EM) signatures of sea ice from initial formation through the development of first-year (FY) ice on the basis of the temporal variations in the physical properties of the ice. The time series of young sea ice signatures, including microwave emissivity, radar backscatter, and visible and infrared spectral albedo, has been measured at successive stages in the growth and development of sea ice, both under laboratory and field conditions. These observations have been accompanied by studies of the physical properties that influence the interaction between radiation and the ice. This has resulted in a consistent data set of concurrent multispectral observations that covers essentially all phases of the development of the different types of sea ice from initial formation to thick FY ice. Mutually consistent theoretical models covering the entire wavelength range of the observations are applied to selected cases and successfully match the observations. Principal component analysis (PCA) of the data set suggests combinations of the set of frequencies to effectively distinguish among different stages in the temporal evolution of the sea ice.**

***Index Terms*—Forward modeling, microwave, optical, sea ice, temporal evolution, thermal infrared (TIR).**

I. Introduction

AN UNDERSTANDING of the electromagnetic (EM) signatures of sea ice is needed to properly interpret satellite and airborne observations of the spatial and temporal evolution of the various ice types. Central to improving the ability to discriminate these types is developing a quantitative description of the influence of the physical properties of the ice on its interaction with EM radiation over a broad range of wavelengths to allow a consistent comparison of imagery from the variety of available satellite sensors. Such a capability offers the potential to improve our ability to assess seasonal, interannual, and long-term changes in the polar ice packs.

Of particular interest for the heat and mass balance of the polar sea ice packs are the spatial and temporal distribution of new and young ice types [1]. These ice types also control, to a large extent, the strength of the ice and its deformation properties over a wide range of spatial scales.

Presently, satellite data are available over a very broad range of wavelengths, from the visible to the microwave regions. Significant progress has been made in identifying sea ice types by various sensors; however, each sensor responds to different ice properties and has individual limitations such that there is no single sensor presently available that does the job by itself. Passive microwave imagers are sensitive to a variety of different ice types and are not appreciably affected by atmospheric conditions, but they are limited by their low spatial resolution. While synthetic aperture radar (SAR) produces high spatial resolution, it is quite sensitive to surface roughness and ice/snow thermodynamics, which can give rise to ambiguities in interpretation. Spatial and temporal coverage is also limited at present. Visible and infrared sensors range in spatial resolution from 10 to 1000 m, but the imagery is strongly affected by solar elevation, cloudiness, atmospheric water vapor, and surface roughness. All of these problems are accentuated when investigating new and young ice types in areas like the Arctic Basin, where the spatial extent of the features of interest are often below the resolution limits of the satellite sensors.

Grenfell *et al.* [2] presented a review of passive and active microwave results, illustrating the variety of ice types that are classified as new and young ice. They showed that radiometric and radar observations can be combined effectively to remove certain ambiguities of interpretation. Elaboration of both passive and active signatures for selected cases of new and young ice were presented by Eppler *et al.* [3] and Onstott [4] in the same volume, but the observational results for new and young ice were limited to a small number of specific

Manuscript received October 31, 1997; revised June 23, 1998. This work was supported by the Office of Naval Research and NASA under Research Grants N00014-89-J-1140, N00014-93-I0149, N00014-95-1-0081, and 3352-PP-0112.

T. C. Grenfell is with the Department of Atmospheric Sciences, University of Washington, Seattle, WA 98195 USA.

D. G. Barber is with the Department of Geography, University of Manitoba, Winnipeg, Man., R3T2N2 Canada (e-mail: dbarber@ms.umanitoba.ca).

A. K. Fung is with the Electrical Engineering Department, University of Texas, Arlington, TX 76019 USA.

A. J. Gow and D. K. Perovich are with the U.S. Army Cold Regions Research and Engineering Laboratory, Hanover NH 03755 USA.

K. C. Jezek is with the Byrd Polar Research Center, Ohio State University, Columbus, OH 43210-1002 USA.

E. J. Knapp and C. T. Swift are with the Microwave Remote Sensing Laboratory, University of Massachusetts, Amherst, MA 01003 USA.

S. V. Nghiem is with the Jet Propulsion Laboratory, California Institute of Technology, Pasadena, CA 91109 USA.

R. G. Onstott and F. Tanis are with the Environmental Research Institute of Michigan, Ann Arbor, MI 48107 USA.

C. S. Roesler is with the Department of Marine Sciences, University of Connecticut, Groton, CT 06340 USA.

Publisher Item Identifier S 0196-2892(98)06662-5.

TABLE I
SENSORS AND THEIR CHARACTERISTICS

E M Observation	Symbol	ν - observation frequency	p - observation polarization	θ - angle of incidence	Instrument
Microwave Brightness Temperature	$T_B(\nu, p, \theta)$, °K	1.414, 2.695, 6.7,10,18.7,37 ,90 GHz	Vertical(V) and Horizontal(H)	30 to 60 deg	Microwave Radiometers
Microwave Emissivity	$e(\nu, p, \theta)$	1.414, 2.695, 6.7,10,18.7, 37,90 GHz	V and H	30 to 60 deg	Microwave Radiometers
Radar Backscatter Coefficient	$\sigma(\nu, p, \theta)$, dB	5,10, 35 GHz	VV, HH, VH, HV	0 to 60 deg	Radar
Spectral Albedo	$\alpha_\lambda(\theta_o)$	400-1000 nm	unpolarized	nadir & zenith viewing, θ_o=solar zenith angle	Spectro-photometer
Thermal IR Emissivity	$e(\theta)$	8-14μm	unpolarized	30-60 deg	Infrared Radiometer
Optical Beam Penetration	K, dB	532 nm	linear	vertical viewing	Laser + Radiance Detector

cases and were not coincident with one another. Since that time, there have been several studies, both observational and theoretical bearing, on these ice types [5]–[10].

Because of the differing responses of the various sensors to different ice types, a useful strategy would be to understand how each sensor type responds and combine instrument-specific data sets to optimize the information retrieval. An analysis along this line was carried out recently [11] for several selected ice types that demonstrated the utility of multisensor combinations.

To this end, an Accelerated Research Initiative (ARI) on the EM properties of sea ice was initiated by the Office of Naval Research. A series of experiments were carried out at the outdoor pond of the Geophysical Research Facility (GRF), United States Cold Regions Research and Engineering Laboratory (CRREL), Hanover, NH, and on thick first-year (FY) ice near Point Barrow, AK, the purpose of which was to investigate the temporal development of the EM signatures for a wide variety of sea ice types. Details of the overall goals and strategy are provided in [12]. The objective of the present work is to carry out a basic comparison of the EM signatures of new and young sea ice types from their formation to their development into FY ice. Our intention here is to provide a basis for defining multisensor algorithms that make use of currently available sensors and formulating more effective algorithms to guide the development of future sensor configurations.

II. EXPERIMENTAL PROGRAM

In the course of the experiments, the time series of new and young sea ice EM signatures, including microwave emissivity, radar backscatter, spectral albedo in the visible and solar infrared, and thermal infrared (TIR) emissivity, has been measured at successive stages in the growth of the ice, both under laboratory conditions and in the field. These observations have been accompanied by studies of the structural properties and near-surface characteristics that influence the interaction between radiation and the ice. This has produced a data set that covers nearly all phases of the development of the different types of FY sea ice classified by the World Meteorological Organization from open water (OW) and new ice to thick FY ice.

The first-stage experiment was carried out at the CRREL outdoor pond from January 19 to 24, 1994 (CRRELEX'94). An ice sheet was grown under quiescent conditions to a thickness of 145 mm over a five-day period. During this time, air temperatures reached as low as −35 °C, simulating Arctic winter growth conditions that, for example, resulted in the release of water vapor from the ice that formed frost flowers at several locations on the surface. Observations with the various sensors were made in continuous rotation to obtain detailed temporal coverage while avoiding crosstalk between the active and passive sensor arrays.

The second-stage experiment was carried out on the sea ice near Point Barrow from April 17 to May 12, 1994 (Barrow'94). In this experiment, thick FY ice was observed with the natural snow cover and with the snow cover removed. The observations provided a comparison with the pond results and made it possible to establish the EM signatures for thick FY ice. Nearly the same set of instruments were used as for the pond experiment, and each ice type was observed sequentially by the full suite of instruments. Since the measurements made during the Barrow experiment are described in detail in an accompanying paper, we show here only selected results to complete the evolutionary sequence [25]. The characteristics of the instruments used and the types of data available are given in Table I.

The physical properties that contribute most strongly to the EM signatures of the ice are the vertical profiles of temperature, salinity, and brine volume, together with the distributions of brine volume, brine pocket, and bubble sizes. Particulate and dissolved materials trapped primarily in the brine pockets are typically also present in sea ice, and their absorption properties can significantly alter the EM signatures. These quantities were all measured during this experiment using well-established techniques. Surface roughness can also have a significant influence for specific sensors; for the cases considered here, the surface roughness was always very small,

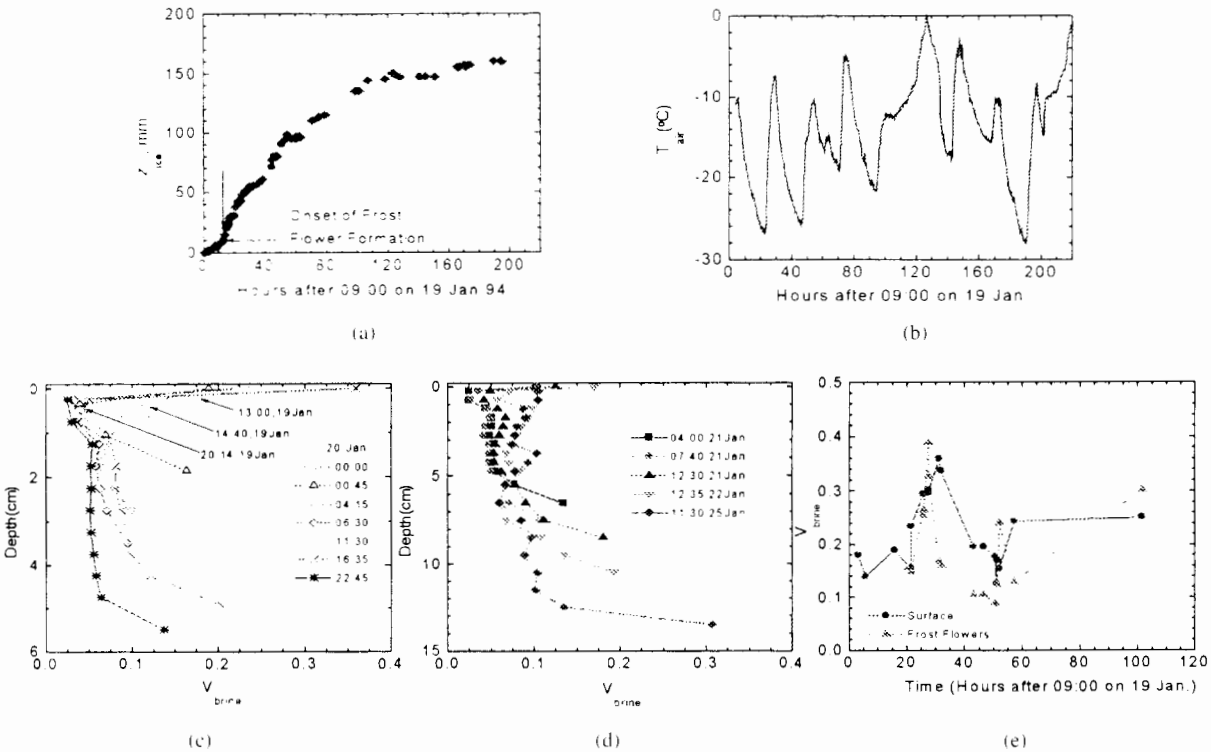

Fig. 1. Physical properties of the ice during the growth phase. (a) Ice thickness (mm) versus time, (b) air temperature (°C) versus time, (c) and (d) brine volume fraction versus depth from January 19 to 21 and from January 21 to 25, respectively, and (e) ice surface (solid line) and frost flower (dashed line) brine volume fraction versus time.

with the general observation that the GRF surfaces were "electromagnetically smoother" than the Barrow sites.

III. Observational Data

Fig. 1 shows the ice thickness and air surface temperature versus time, together with the brine volume profiles measured during the growth phase. Growth was steady throughout the experiment, but it slowed continually as the ice thickened. At approximately 13 h after the start of the ice growth, frost flowers began to form on the surface as a result of moisture released into the cold air that then caused riming. The frost flowers formed in small patches on the surface that gradually increased in size and thickness but never fully covered the ice. Thus, it was possible to study bare and frost-flower-covered areas concurrently. The crystallographic characteristics and the specification of brine and bubble size distributions for selected cases have been presented by Perovich and Gow [13] and are not repeated here.

In addition to the properties of the ice itself, other absorbers are present, in general. Of these, the most important for specifying the inherent optical properties of the ice are particulate and dissolved organic material in the seawater that became incorporated into the ice as it grew.

Because of the overwhelming contribution to volume scattering by brine inclusions, vapor bubbles, and ice crystals, scattering by the particulate material is assumed to be negligible for visible wavelengths. This material is also neglected in our microwave models because the particles are very small (<30 μm) compared to microwave wavelengths, and they have a very weak dielectric contrast with respect to the brine inclusions. We assume the same thing about the dissolved material because, at microwave frequencies, it will affect the bulk properties of the brine and the brine volume fraction very little.

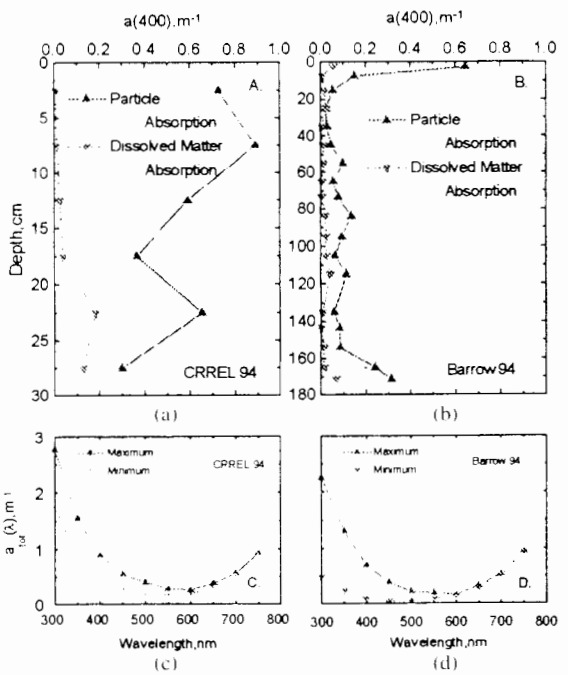

Fig. 2. Absorption coefficients of sea ice, including embedded particulates and dissolved material. (a) $a_p(400)$ and $a_d(400)$ for CRRELEX'94, (b) $a_p(400)$ and $a_d(400)$ for Barrow'94, (c) maximum and minimum values of $a_{tot}(\lambda)$ for CRRELEX'94, and (d) maximum and minimum values of $a_{tot}(\lambda)$ for Barrow'94.

Consequently, we characterize the particulate and dissolved components by their measured optical absorption. Presented in Fig. 2 are depth profiles of the absorption coefficients at

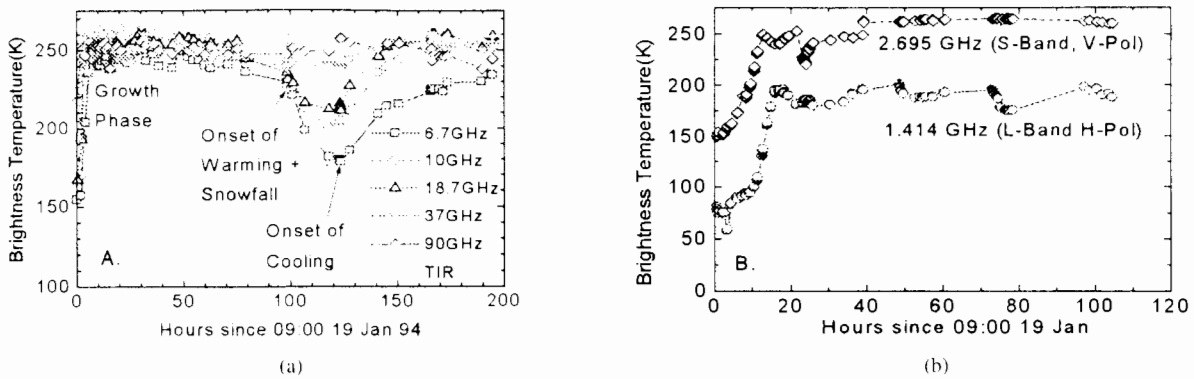

(a) (b)

Fig. 3. Microwave and TIR brightness temperature evolution from OW to 15-cm thick young ice. Nadir angle = 50°: (a) 6.7 to 90 GHz and TIR and (b) 1.414 and 2.695 GHz.

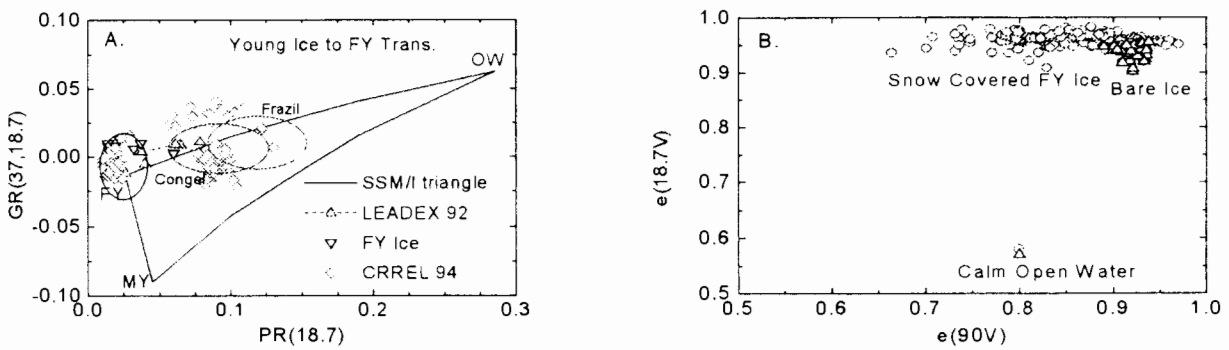

(a) (b)

Fig. 4. Scatter plots of (a) PR versus GR and (b) e(18.7 V) versus e(90 V) for young ice and FY ice cases. In (a), the vertices of the triangle—OW, FY, and multiyear (MY)—refer to the assigned "tie points" for OW, FY ice, and MY ice. Given in the legend are the sources for the various data sets. The ovals labeled "Congel" and "Frazil" give the location for observations of young congelation ice from five previous experiments [38] and for observations of frazil ice from the CRRELEX'95 experiment, respectively [38]. The large triangle in (a) shows the region containing linear mixtures of OW, FY ice, and MY ice.

a wavelength of 400 nm, both for particulates $a_p(400)$ and for dissolved material $a_d(400)$, measured at CRREL and at Point Barrow. Also included are the maximum and minimum curves for spectral absorption$a_{\rm tot}(\lambda)$ of the bulk medium, including ice, particulates, and dissolved material. At visible wavelengths, absorption is dominated by the particulate and dissolved components, while in the infrared, the ice absorption increases rapidly and becomes the dominant absorber.

A. Passive Microwave Observations

Selected passive microwave data obtained during the growth of the ice sheet are shown in Fig. 3. These data consist of brightness temperatures (T_B) at frequencies from 1.4 GHz (L-Band) to 90 GHz (W-Band). The T_B values shown are primarily for vertical polarization (V-pol), except for the L-Band, and TIR observations, which are for horizontally polarized (H-Pol) and unpolarized radiation, respectively. As seen in prior experiments [2], [14], the brightness temperatures rose rapidly as the ice thickness increased from the low initial values characteristic of OW to saturation levels for optically thick saline ice. The physical thicknesses at which the ice became optically thick were greatest for the lowest frequency, approximately 4–5 cm at L-band, and decreased at higher frequencies to about 2–3 mm at 90 GHz. Subsequent variations up to about 120 h were due to diurnal atmospheric forcing of the thermodynamic characteristics of the surface and volume of the growing sea ice. These can be seen most easily in the L-Band data.

At approximately 110 h, a light snowfall began that deposited 2.5 cm of snow onto the ice. This was accompanied by an upward shift in the diurnal air temperature pattern and caused some melting in the snow. At about 140 h, the air temperature went through a maximum and began to cool. The resulting spread in T_B seen in Fig. 3 was a result of the frequency dependence of absorption in the wet snow, such that the deepest and coldest layers contributed to T_B only at the lower frequencies, while the warmer upper layers contributed at the higher frequencies.

Of particular interest is the transition from young ice to FY ice for the passive microwave signature interpretation, shown by the observations plotted in Fig. 4. Fig. 4(a) is a scatter plot of polarization ratio (PR = $[T_B(18.7\ \text{V}) - T_B(18.7\ \text{H})]/[T_B(18.7\ \text{V}) + T_B(18.7\ \text{H})]$) versus gradient ratio (GR = $[T_B(37\ \text{V}) - T_B(18.7\ \text{V})]/[T_B(37\ \text{V}) + T_B(18.7\ \text{V})]$). Fig. 4(b) shows a comparison of scatterplot results for e(18.7) versus e(90) for young and FY ice.

The deposition of the snow and its subsequent metamorphism gave rise to a shift in PR from values near 0.1 to values of about 0.025. At the same time, the snow introduced irregular zones with varying structure, thickness, and grain size, which resulted in fluctuations in volume scattering. This spread out the FY ice cluster parallel to the e(90) axis such that e(90) was lower for areas of greater scattering, while e(18.7) remained

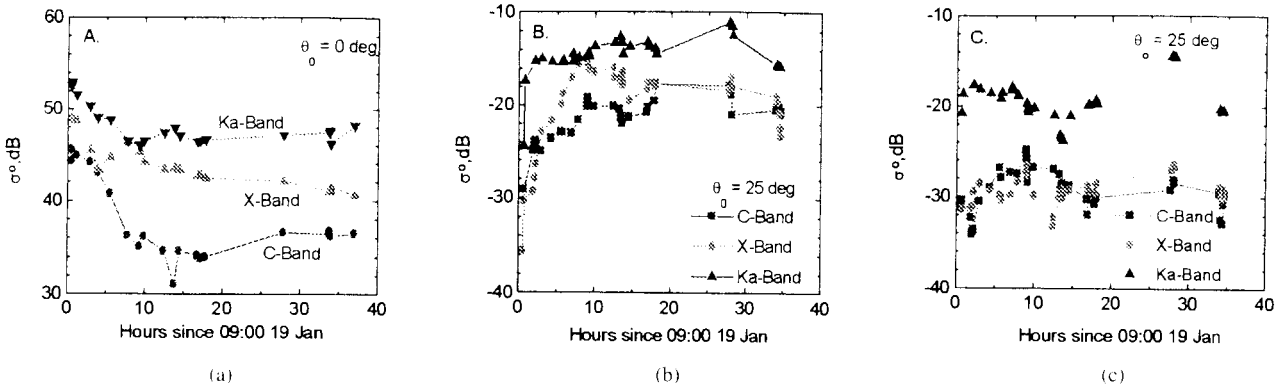

Fig. 5. Coherent radar backscatter observations during new/young ice growth at C- (5.3 GHz), X- (10 GHz), and Ka-bands (38 GHz): (a) nadir viewing, (b) nadir angle 25°, H-pol, and (c) nadir angle 25°, cross polarization.

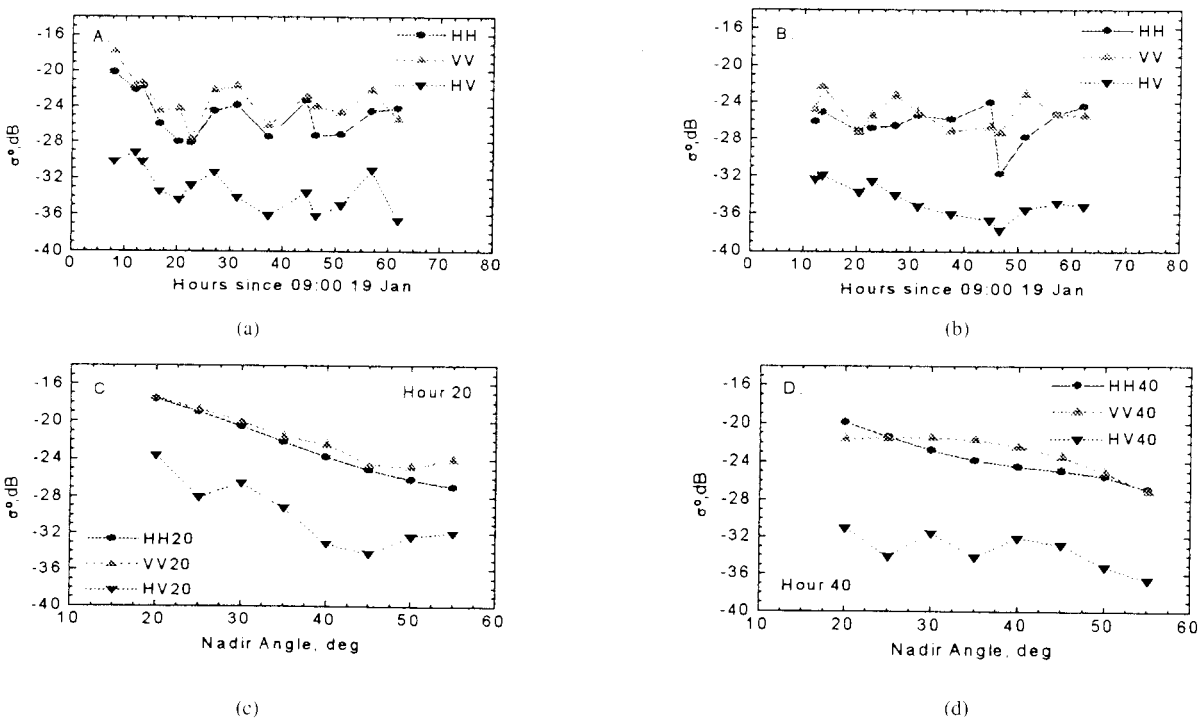

Fig. 6. Backscattering coefficients (σ^o) at C-band during ice growth. (a) Multipolarized results at a nadir angle of 35°, (b) multipolarized results at a nadir angle of 50°, (c) angular dependence at 20 h, and (d) angular dependence at 40 h. The center frequency was 5 GHz, the bandwidth was 1 GHz, and the instrumental beamwidth was 12°.

essentially unchanged. It is clear that the introduction of the snow cover is what distinguishes young ice types from FY ice [5], [15], [16].

B. Active Microwave Observations

Radar backscatter observations carried out over the first 70 h of the experiment are shown in Fig. 5. Nadir-viewing observations at C-, X-, and Ka-bands show a significant decrease in backscattering coefficient (σ^o) between 0 and about 20 h, corresponding to a decrease in the effective permittivity of the ice/water system. This was accompanied by a strong increase at a nadir angle of 25° as the ice thickness increased and the character of the surface developed. This occurred over about the same time interval as the increase in T_B at the same frequency bands. Cross-polarized values ranged from 5 to 10 dB below the like-polarized values.

Observations were also made at 5 GHz [Fig. 6.] of σ^o_{VV}, σ^o_{HH}, and σ^o_{VH}, beginning at about 9 h after initial ice formation. These observations showed a decrease with time due to a decrease in the near-surface brine volume. Superposed on this was a diurnal signal associated with period solar heating of the ice that modified the near-surface brine volume. A detailed study of this phenomenon has recently been published [17]. The diurnal signal is also apparent in the passive microwave results with a magnitude of 8–10 K. The angular dependence of σ at 20 and 40 h showed a decrease of about 8 dB between 20 and 55° for like-polarizations. At 20 h, the cross-polarized signal was 6–9 dB below the like-polarized value. At 40 h, this difference had increased to about 10–12 dB. At the same time, the like-polarized values decreased 2–3 dB at 20°, but they remained about the same at 55°. This suggests that the surface had become slightly smoother, but that a small amount of volume scattering is present. It appears that the two

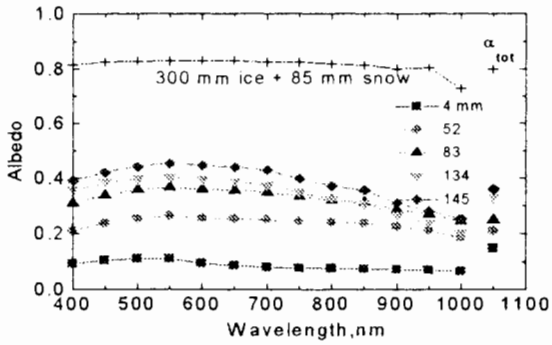

Fig. 7. Evolution of spectral and total shortwave albedo from young ice to FY ice during CRRELEX'94. Clear skies, $\theta_{sun} = 60^{\circ}$. Ice thickness in millimeters is indicated in the legend.

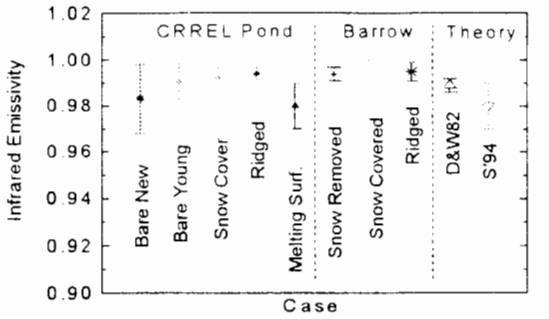

Fig. 8. TIR emissivities for the indicated ice types observed at 50° nadir angle at the CRREL Pond and at Point Barrow, AK. Model results for snow are from Dozier and Warren [18]. For pure ice, they have been computed from the data of Salisbury *et al.* [19].

sets of radar results are consistent. For like polarization, the uncertainties appeared to be 2–3 dB for the values shown in Fig. 5 and about 1 dB in Fig. 6.

C. Albedo Observations

The temporal development of spectral albedo (α_λ) during the ice growth is shown in Fig. 7. The lowest values, observed for new ice, were approximately 0.08 across the spectrum, with a slight maximum at 500 nm. As ice thickness increased, α_λ increased at all wavelengths, with a maximum at about 550 nm. The highest values for bare ice were measured at a thickness of 145 mm.

Although α_λ had not yet reached saturation, ice growth in the pond slowed considerably and surface modification had begun to develop, so the sequence was terminated at that point. The solid curve for 300-mm ice covered with 85-mm snow was obtained on a thicker sheet grown just prior to the growth experiment. The major difference between the two cases is the influence of the highly scattering snow layer. This is representative of the change that takes place during the transition from young ice to FY ice, although the underlying ice is usually thicker in field situations.

D. TIR Observations

TIR emissivities were obtained concurrently with the passive microwave data. Since the range of observed values is comparable to the uncertainties, we present examples for characteristic surface types (Fig. 8) rather than a time sequence. The lowest values obtained were about 0.98 for bare new ice with a high salinity surface layer and for ice with a melting surface. For all other surface types, values ranged from 0.99 to 0.996, showing a trend for increasing mean values and reduced uncertainty with increasing ice age/thickness. The principal physical effect was due to the presence of a smooth, thin liquid layer on the new and melting ice that increased the Fresnel reflectivity of the surface and thus lowered the emissivity. The rougher or granular natural surfaces for which this layer was absent had higher emissivities.

Shown for comparison are spectrally averaged values for snow from Dozier and Warren [18] together with emissivities for ice determined from the results of Salisbury *et al.* [19]. The latter calculations are for pure ice with a smooth upper surface, however, they should apply reasonably well to saline ice because the dielectric properties of ice and brine do not differ strongly between 8 and 12–14 μm. Indeed, the theoretical results are consistent with observations in both cases.

E. Comparison of Pond and Field Data

In an effort to compare data obtained in the field and at the pond, we show in Fig. 9 selected passive microwave and spectral albedo results. For the passive microwave, each of the points represents an average of over 20 sites. For both bare and snow-covered ice, the points in the PR–GR plot coincide to within one standard deviation. The spectral albedos show about the same increase with the addition of a snow cover, but the paired curves for bare and snow-covered ice are significantly different, particularly at wavelengths less than 700 nm. As a result, the pond ice appears "greener" than the natural ice. This is likely due to the enhanced concentrations of absorbing particulate and dissolved materials trapped in the ice [Fig. 2(b)]. While the ice near the surface of the pond ice exhibited absorption coefficients at 400 nm, comparable to those measured in the field, the absorption coefficients remained elevated throughout the pond ice column compared to those measured in the Point Barrow ice core. The entrapped material, consisting primarily of particulates, was characterized by large absorption coefficients in the ultraviolet, which decreased exponentially toward the red end of the spectrum. This is characteristic of particulate organic material [20]. In combination with the absorption coefficients for pure ice [21], [22], these organic materials give an absorption minimum between 550 and 600 nm compared to 450–500 nm for the Point Barrow ice [Fig. 2(b)]. Consequently, the albedo differences between the pond and field experiments appear to be due, in large part, to the differences the spectral absorption coefficients.

For the visible wavelengths, the ice is not optically thick and, thus, the physical thickness of the ice is important. The optical properties of the underlying water column can also can alter the albedo, primarily for the thinner ice types. In addition, the pond ice was characterized by a much thinner surface granular layer compared to that of the thick FY ice (<2 versus 8 cm) This would result in additional reduction of the optical thickness for the pond ice relative to the FY ice. At longer wavelengths, however, where the ice is optically thicker, the albedo curves are quite similar. Consequently, the differences between the pond and field experiments appear to

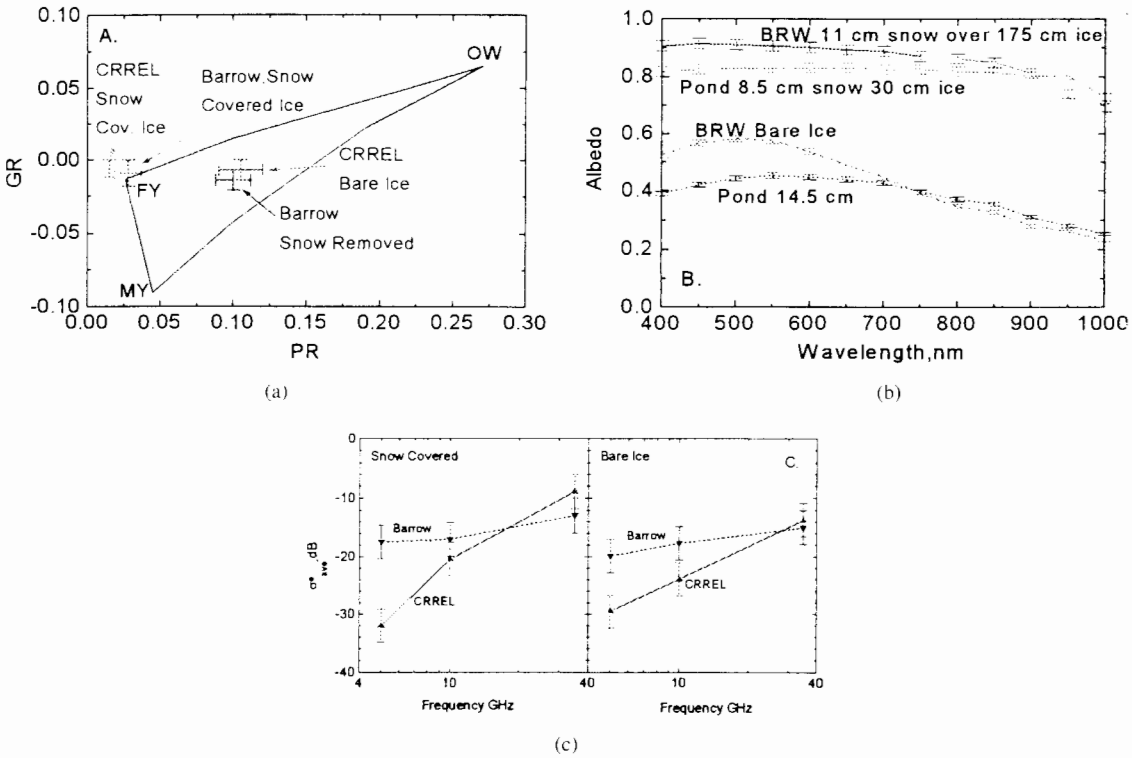

Fig. 9. Comparison of CRRELEX'94 pond results and field data from Barrow'94: (a) passive microwave PR-GR observations. The error bars denote one standard deviation; (b) spectral albedo observations; and (c) radar backscatter spectra at 27° nadir angle. Average of σ_{VV} and σ_{HH} with rms error.

be due to the differences in the thicknesses of the ice and snow layers and the variations in the inherent optical properties. This is consistent with the modeling results in the next section.

The radar backscatter results for the pond and the field are not significantly different at 35 GHz. For the pond case, however, σ^o drops off more steeply with decreasing frequency than for the Point Barrow observations. This can be explained by assuming that at Point Barrow there was surface roughness with a horizontal correlation length in centimeters and a larger range resulting in a rather gradual increase with frequency, while at the pond there was only very small scale roughness that increased strongly with frequency. This is consistent with the observed degrees of surface roughness in the two experiments.

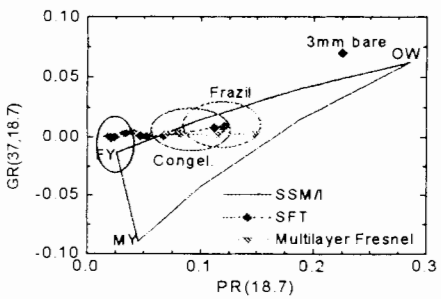

Fig. 10. Theoretical model results of the transition of the passive microwave PR-GR signature from young to FY ice. Results for the SFT model are given by the diamonds. The multilayer Fresnel results are indicated by inverted triangles. The ovals indicate the observed regions for young frazil, young congelation, and FY ice, respectively.

IV. Theoretical Modeling

A. Microwave Emission

Several different models are applied below whose optimal application depends on the wavelength range and type of observation under consideration. Each of these models is described in more detail in [23] and [24]. In all cases, however, the physical properties of the ice were constrained by detailed characterization of the physical properties of the ice and of the ambient thermal and radiative environment that were measured concurrently [25]. Although the individual models contain certain parameters, which were not measured and thus had to be estimated, the above constraint provided a common connection among the models.

To investigate the passive microwave signature transition from bare young ice to FY ice, we applied a multilayer strong fluctuation theory (SFT) model. This is a wave model that represents the ice and snow as effective random media in which the vertical variations in brine volume and density and, hence, relative permittivity and scattering properties are represented by a series of discrete interacting layers [5]. The model represents young ice as a homogeneous layer covered with a 25-mm-thick slush layer. The slush was allowed to cool from -5 to -20 °C, as observed, and the corresponding value of PR decreased from 0.12 to 0.047. Adding 10 mm of dry snow decreased PR to 0.031, and allowing the cooling to continue to -25 °C reduced PR to 0.021. Throughout this sequence, shown in Fig. 10, GR decreased slightly from 0.009 to 0.001 as a result of the slight increase in volume scattering. These values spanned the observed range of variation for the transition from young ice to FY ice.

An alternate study of the same transition using a multilayer Fresnel model [26] produced similar results, as shown. In that case, the young ice was modeled as having a surface brine

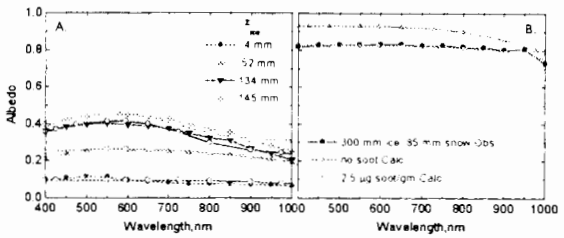

(a) (b)

Fig. 11. Comparison of radiative transfer model calculations with spectral albedo observations versus ice and snow thickness: (a) bare ice from 4- to 145-mm thickness and (b) 300-mm-thick ice with 85-mm snow and 85 mm of snow plus 2.5-μg soot/g.

slick with a brine volume of 20% that decreased upon cooling. When PR reached 0.8, a layer of frost flowers was introduced that increased in density and wicked up brine from the surface, reaching a final PR value of 0.04. In this case, GR the values were essentially constant at 0.003.

In order to achieve the decrease in PR, it was necessary in both cases to introduce a low-density layer at the surface. This layer produced a more effective impedance match that reduced the coherent reflectivity at both V- and H-pol, thus reducing PR. This is consistent with the observations of young ice and FY ice, in which the young ice has a high-salinity, slushy surface layer and ice with a FY signature has a continuous, snow/frost layer several centimeters in thickness.

B. Visible/Infrared Albedo

To investigate the spectral albedo observations, a four-stream, multilayer, discrete ordinate radiative transfer model was applied. This model has been used successfully in studies of Antarctic snow [27] and has been designed specifically for use with sea ice [28]. Between three and seven layers, depending on the total thickness, were used to represent the vertical variations in inherent optical properties of the ice and snow.

The comparison for five individual cases is shown in Fig. 11. In each case, the presence or absence of a cloud cover was taken into account explicitly in the calculations. The ice structure was specified by the observed absorption, salinity, temperature, density, and embedded material profiles [13], [29]. For the bare ice cases, initial comparisons underestimated the albedos across the spectrum for all but the 4-mm-thick ice. The discrepancy was typically 0.02 between 400 and 600 nm, but it increased to almost 0.2 at 1000 nm. To account for this, we assumed the existence of a frost or trace snow layer on the surface between 0.5 and 0.9 mm in thickness. Such a layer would not be readily visible and was consistent with occasional light snow flurries that occurred during the experiment.

The resulting fits were achieved using the observed constraints on the ice structure. On average, the agreement was acceptable; however, the wavelength dependence was unrealistic. Adjusting the physical properties of the ice within the observational uncertainties did not improve the agreement significantly, and it was necessary to incorporate the absorption coefficients of the entrapped material, as shown in Fig. 2. The results are shown in Fig. 11 and fit the observations much better, particularly from 400 to 500 nm.

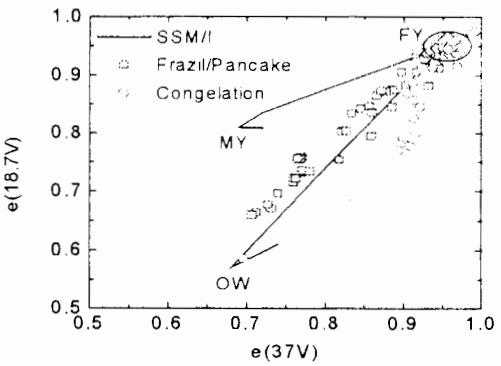

Fig. 12. Scatter plot of e(18.7, V-pol) versus e(37, V-pol) for congelation and frazil/pancake ice during the development from OW to young ice. FY ice region enclosed by the ellipse is included for reference.

For the thicker snow-covered ice, the observations could not be explained with an 8.5-cm-thick layer of pure snow. Reducing the layer thickness to 2.5 cm produced a very good match, but this was not consistent with the actual snow thickness. By assuming the presence of small amounts of soot in the snow scavenged out of the atmosphere, we were able to explain the discrepancy. Using the optical properties for soot of Warren and Wiscombe [30], a concentration of 2.5 μg/g matches the observations quite well. Although the soot concentration in the snow was not measured, and observed albedos would vary with differing vertical distributions of the soot, 2.5 μg/g is not an unreasonable level for the pond environment. Embedded impurities in the ice were included in the calculations but produced an albedo change of less than 0.01 at 400 nm.

V. Comparison with Other Observations

To indicate how representative the present results are of sea ice in general, it is useful to relate them to observations collected during other experiments on similar ice types. An alternate evolutionary sequence occurs, for example, when sea ice grows in wavy, wind-roughened water producing frazil and then pancake ice. While a detailed treatment of this topic is provided by Onstott *et al.* [31], it is an important component of the signature evolution, and some mention of the differences is appropriate in the present context.

Fig. 12 shows scatter plots of microwave emissivity at 18.7 and 37 GHz for V-pol during the growth of pancake ice at the CRREL pond in 1995 and congelation ice from 1994. The two sequences are different during the early stages, to thicknesses of a few centimeters, but they converge as the ice grows thicker to the values found for FY ice. This indicates that, although there are significant differences in ice salinity and in surface roughness, these two situations converge to almost the same emissivities and retain these values throughout the growth of FY ice.

A related comparison is given in Fig. 13 for scatter plots in PR–GR space. This plot combines results from the present experiments with previously reported results for similar ice types [5], [15], [16], [32]. The evolutionary paths are again quite different for congelation and frazil/pancake ice types. As above, both sequences quickly converge into confined regions

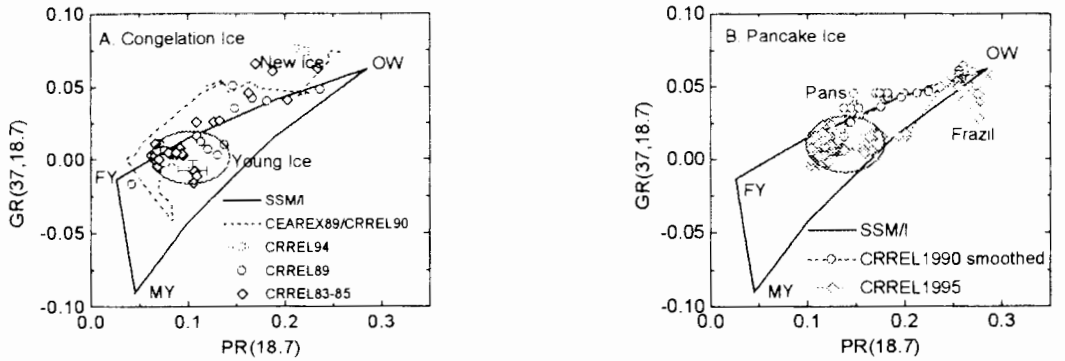

(a) (b)

Fig. 13. (a) GR-PR data from various experiments showing the signature evolution from OW through young ice for both congelation and (b) pancake ice. The ellipses show the regions of convergence for young ice.

indicated by the ellipses. In this case, however, the PR values are about 0.04 greater for the pancake ice, so the difference is due to variations in e(H-pol).

A sensitive indicator of the volume-scattering properties of sea ice at visible wavelengths is the beam attenuation. This quantity relates directly to the attenuation of a direct solar beam under clear skies. During experiments conducted in January 1993 and 1994, beam transmission observations were made. Although we do not have a detailed series during the 1994 experiment, the data from the previous year for similar ice growth conditions provide a picture of temporal evolution.

The data were obtained over a range of ice thicknesses using a Nd:YAG laser mounted beneath the ice together with a 2° field-of-view radiance detector positioned 2 cm above the ice. In 1993, measurements were made during the first 40 h of ice growth until the ice reached at thickness of 56 mm. The beam transmission of the ice layer versus ice thickness together with the beam attenuation coefficients derived for three separate growth intervals is shown in Fig. 14. After the first 4 h of ice growth, the beam transmission had decreased to −16.4 dB ($T_{\rm ice} = 0.0229$), implying an average beam attenuation coefficient ($K_{\rm beam}$) of 3.8 cm^{-1}. Between thicknesses of 10 and 25 mm, $K_{\rm beam}$ decreased to 1.6 cm^{-1} and, at the end of the sequence, it had reached 0.4 cm^{-1}. In 1994, the measurements were repeated but only for bare 310-mm-thick ice. In this case, $K_{\rm beam}$ was determined to be 0.38 cm^{-1}, very close to the value determined at the end of the sequence for the previous year.

The general decrease in beam attenuation coefficient with increasing ice thickness is primarily a result of the lengthening and alignment of the ice crystals giving rise to reduced volume scattering in the layers below the surface. This general relationship between optical transmission and ice evolution during the early stages of ice growth was observed in several other experiments and is consistent with vertical variations in the structure of the ice [13].

VI. Discussion

The overall agreement between the observations and models shows that, even though the model parameters were not fully constrained, it was possible to achieve a good match between theory and observation with reasonable values of the inherent

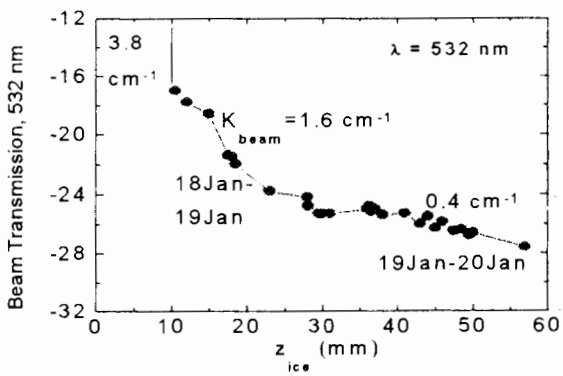

Fig. 14. Beam transmission for new and young ice of varying thicknesses at 532-nm wavelength. Total beam attenuation coefficient values for the initial intermediate and final conditions are shown.

optical properties that were in turn consistent with the observed physical properties. The model results also provide a link that indicates consistent behavior among the assembly of different sensors for the ice types considered here.

Another important benefit of the present model comparisons is to identify the aspects of the structure that are important for the variations observed by the different sensors. For example, in the visible and near infrared, the dominant factors are the ice thickness, the brine volume profile $V_b(z)$, the snow thickness, the snow grain size, and the absorption by entrapped material.

The observed albedo maximum occurred at 600 nm in the pond cases considered here, consistent with the enhanced absorption coefficients in the near-ultraviolet and blue regions of the spectrum due to particulates and dissolved matter. Field observations from FY ice near Point Barrow indicate that the reduced concentrations of entrapped materials in the surface ice were accompanied by "bluer" albedo spectra [20], [33]. In the absence of such absorbing material, the predicted maximum albedo would be shifted to about 470 nm for both bare and snow-covered cases, as observed for snow on the Antarctic Plateau [27].

Passive microwave emissivity is sensitive to variations in the bulk dielectric properties throughout the ice and snow and thus depends strongly on $V_b(z)$—or liquid fraction. Scattering can also be significant, primarily at higher frequencies, so the snow grain size is also important. The relative influence of these parameters shifts with observed frequency. At lower

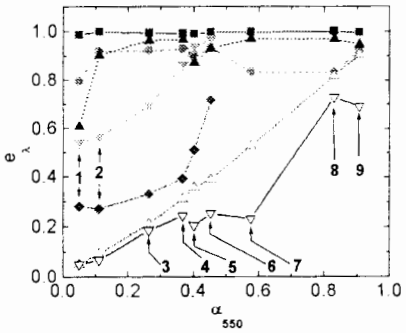

Fig. 15. Selected microwave emissivities [e(90 V) filled circles, e(18.7 V) filled up triangles, e(2.6 V) filled down triangles, e(1.4 H) filled diamonds], infrared emissivity [filled squares], α_{400} [open up triangles], and α_{1000} [open down triangles] versus α_{550} for all ice cases specified in Table II.

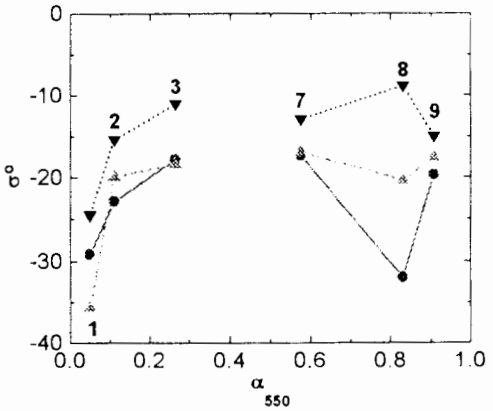

Fig. 16. Radar backscattering coefficients at 25° incidence at C-band (diamonds), X-band (up triangles), and Ka-band (down triangles) versus α_{550} for the six ice cases indicated. The curve designations correspond to those in Fig. 15.

frequencies, scattering by the snow grains is negligible and the emissivity is dominated by the details of $V_b(z)$. The radiation penetration depth decreases rapidly with increasing frequency, and at 37 and 90 GHz, only the uppermost few millimeters or centimeters of the ice contribute to the emitted radiation, while volume scattering by the snow can become substantial. Note that fine-grained new snow produces rather little volume scattering and grain metamorphism gives rise to the situations in which volume scattering is strong [27], [34]. A more detailed quantitative investigation of the role of a snow cover on the microwave signatures of sea ice is presented by Barber *et al.* [35].

The radar backscatter at nadir incidence also depends primarily on the dielectric structure of the ice, but its modulation includes a substantial contribution from surface and interface roughness in addition to volume inhomogeneities. At oblique incidence, the surface roughness is even more important.

TIR emissivities depend only on the physical properties of the upper surface, primarily the geometry of the surface layer rather than the presence or absence of a surface brine layer or particulate or dissolved materials. This is because the radiation penetration depth near 10 μm is on the order of 10^{-2} mm in ice. Thus, the dominant determining factor is surface roughness for bare ice or scattering by the uppermost layer of grains in snow. The observations indicate that the emissivity is lowest for the smooth surfaces and that even a small amount of roughening raises the values very close to 1.0.

To illustrate the extent to which the observations correlate with the albedo at a wavelength in the middle of the visible region, we show in Figs. 15 and 16 plots of selected sets of EM data versus α_{550}. The set of ice cases available for the comparison are described in Table II, along with the corresponding α_{550} values. These cases range from growing bare new and young ice (Cases 1–5) to thick FY ice with and without its natural snow cover (Cases 7 and 9). Cases 6 and 8 are thicker pond ice with a snow cover.

Table III gives the correlation coefficient R for the observations shown in Fig. 15 relative to α_{550} in order of decreasing correlation coefficient R. The albedo at 400 nm correlates most strongly, which is consistent with predictions of the radiative transfer model. α_{1000} shows a somewhat lower correlation because it depends only on the ice conditions in the upper few centimeters rather than throughout the full ice thickness.

TABLE II
ICE/SNOW CHARACTERISTICS

Case	Ice Thickness	Snow Thickness	α_{550}
1	0 mm/ trace	0 mm	0.05
2	4 mm	0 mm	0.11
3	50 mm	0 mm	0.26
4	80 mm	0 mm	0.37
5	135 mm	0 mm	0.40
6	145 mm	20 mm	0.45
7	1.7 m	0 mm	0.58
8	0.31 m	85 mm	0.83
9	1.7 m	0.12 m	0.91

TABLE III
INTERSENSOR CORRELATION COEFFICIENTS RELATIVE TO α_{550}

Channel	R	Probability that R=0
α_{400}	0.997	<0.0001
e(2.6V)	0.984	0.0003
α_{1000}	0.938	0.0002
e(1.4H)	0.849	0.033
e(18.7V)	0.58	0.10
e(TIR)	0.55	0.12
e(90V)	0.036	0.93

Passive microwave emissivities correlate less strongly with albedo as the frequency increases, the result of decreasing penetration depth of the radiation. Our present results suggest that low-frequency radiometry in the L- and S-band range would be best suited to predict α_{550} and presumably ice thickness as well up to a saturation thickness, approximately 20–50 cm, depending on ice salinity. Unfortunately, we do not have L- and S-band results for the thick snow-covered ice cases. Previous results [2], [14], [36] indicate, however, that these frequencies are not sensitive to snow cover and the subsequent behavior of the emissivity depends on the evolution of the brine volume profile.

The correlation at 90 GHz is calculated to be very weak because the positive correlation for thin bare ice is offset by an anticorrelation for thicker snow-covered ice. This arises

TABLE IV
SENSOR COMBINATIONS INDICATED BY PCA ANALYSIS

Range of Cases	Sensors Available	Principa l Comp.	% of Total Variance Explained	VIR	PMW	AMW
1 - 9	VIR & high freq. PMW	#1	79.5	α_{400} or α_{550}	e(18.7) or e(37)	n.a.
		#2	15.4	α_{400} or α_{550}	-e(18.7) or -e(37)	n.a.
		#3	2.6	$[\alpha_{550} - \alpha_{1000}]$	[e(18.7V)-e(6.7V)] or [e(18.7V)-e(18.7H)]	n.a.
1 - 6	VIR & all PMW	#1	66.5	α_{400} or α_{550}	e(H-pol) or PR	n.a.
		#2	31.5	$[\alpha_{400} - \alpha_{1000}]$ or $[\alpha_{550} - \alpha_{1000}]$	e(1.4H)-e(6.7H) or e(1.4H)-e(18.7H)	n.a.
		#3	1.3	α_{400} or α_{550}	e(6.7)-e(90)	n.a.
1 - 3, 7 - 9	VIR & AMW	#1	87.6	α_{400} or α_{550}	n.a.	$\sigma_s(X)$ or $\sigma_s(Ka)$
		#2	8.9	α_{1000}	n.a.	$-\sigma_s(C)$ or $-\sigma_s(X)$
		#3	2.7	$[\alpha_{400} - \alpha_{1000}]$ or $[\alpha_{550} - \alpha_{1000}]$	n.a.	$[\sigma_s(Ka) - \sigma_s(X)]$ or $[\sigma_s(X) - \sigma_s(C)]$
1 -3, 7 - 9	VIR, high freq. PMW, AMW	#1	78.7	α_{400} or α_{550}	e(18.7) or e(37)	$\sigma_s(X)$ or $\sigma_s(Ka)$
		#2	16.7	α_{400} or α_{550}	[e(90) - e(6.7)]	$-\sigma_s(X)$ or $-\sigma_s(Ka)$
		#3	2.8	$[\alpha_{400} - \alpha_{1000}]$ or $[\alpha_{550} - \alpha_{1000}]$	[e(90) - e(37)]	$[\sigma_s(Ka) - \sigma_s(X)]$ or $[\sigma_s(X) - \sigma_s(C)]$
1 - 3, 7 - 9	High freq. PMW, AMW	#1	85.8	n.a.	e(H-pol) or PR	$\sigma_s(X)$ or $\sigma_s(Ka)$
		#2	10.9	n.a.	[e(37) - e(6.7)]	$[\sigma_s(Ka) - \sigma_s(X)]$ or $[\sigma_s(X) - \sigma_s(C)]$
		#3	2..5	n.a.	[e(90) - e(37)]	$[\sigma_s(Ka) - \sigma_s(X)]$
Recommended				α_{vis}	e(intermed. freq.)or PR	$+\sigma_s$
				$[\alpha_{vis} - \alpha_{1000}]$	[e(low freq.) -e(inter.freq.)]	$-\sigma_s$
				$[\alpha_{550} - \alpha_{1000}]$	[e(90) - e(37)]	$[\sigma_s(high) - \sigma_s(low)]$

because in the initial growth stages both albedo and emissivity increase together, but the snow cover and evolving structure of the upper layers of the thicker ice produce increased volume scattering that reduces e(90) but increases the albedo. e(TIR) depends only on the conditions at the surface and is very close to unity in all cases. Since the uncertainty in these variations is typically smaller than the experimental uncertainties (see Fig. 8), we have not attempted to refine the correlation analysis at this point.

The situation with respect to the radar results is somewhat different. During new/young ice growth, $\sigma^o(25^\circ)$ increases with α_{550}, as do the microwave emissivities, and there is a strong correlation between σ^o and albedo; however, the correlation becomes very weak for the thicker ice types. This behavior is a result of changes in the surface roughness that occur throughout the growth and development of the ice. Saturation with respect to ice thickness occurs for z_{ice} slightly greater than 50 mm.

For the thick and snow-covered ice, values of σ^o depend on how large the scatterers are and on the layer structure of the upper part of the ice and the snow. Case 8, for example, shows very low values of σ^o at C-band with a rapid increase at higher frequencies, characteristic of a Rayleigh scattering response for a snow grain size that is small compared to the wavelength. Case 9, also a snow covered site, shows quite different behavior. Here our model results indicate that the snow acts as an impedance matching layer because it contains a dielectric gradient due to vertical salinity and density gradients in the snow. This reduces the effective reflectivity of the system. As a result, scattering decreases, as described above, and much of the radar wave is transmitted into the ice that would be backscattered if the dielectric discontinuity were more abrupt.

VII. PRINCIPAL COMPONENT ANALYSIS

In order to explore intercomparison of sensors to determine optimal combinations that span the data set defined in Table II, a principal component analysis (PCA) was carried out. The set of cases was chosen such that all the spectral albedo observations were included. The analysis was a supervised PCA [37] of a small but well-defined data sample. Since not all sensors were used for all nine cases, several separate analyses were carried out on subsets of the data.

Because of the small data set available, which leaves out a number of natural ice types, we employ this technique primarily to indicate which combination of sensors would be most effective on the basis of the present data set in distinguishing ice type. Rather than presenting a specific algorithm, we present a combination of channels suggested by the analysis that spans the present data space efficiently. To test whether these combinations are effective for general remote sensing, they should be applied to larger data sets, such as those produced by aircraft and satellite platforms.

In Table IV, we present results from five separate PCA analyses, showing parameters for each sensor that can be used to form a linear combination that approximates the particular principal component. The table gives the range of cases included in each analysis, as specified in Table II, the sensors for which data are available for that case, the first three principal components, the fraction of the total variance

explained by each, and the channels that can be combined to represent each principal component. The channels include α in the visible and near infrared, e for the passive microwave, and scaled backscatter coefficients σ_s for the active microwave. To meet the assumptions of scale invariance, required by the PCA, we applied a linear scaling factor to the σ_s to ensure that it covered the same dynamic range as albedo and emissivity.

Linear combinations of the sensor channels given are designed to discriminate effectively among the different ice types. When an "or" is specified, it implies that intermediate wavelength or frequency observations can be substituted with essentially no degradation in variance explained. An ice-type algorithm based on this information would use as variables the linear combinations of the sensor channels for each principal component for a given case. The coefficients of the linear combinations would be determined using the data set under analysis.

The PCA analyses indicate that a variety of sensor combinations can resolve the growth of new and young ice. The deposition and subsequent development of a snow cover also produces clear changes, most notably due to its effect on spectral albedo, but also due to the responses of the passive and active microwave. Thus, we have been able to resolve the growth and development of the full range of ice cases studied here.

VIII. Conclusions

The multifrequency, multisensor data set presented here shows the evolution of the EM signatures of sea ice from formation to thick FY ice. Due to the large range of penetration depths at different observational frequencies, the signatures of the various sensors respond to changes at various levels in the evolving ice. As a result, the correlation among sensors spans a wide range. Where sensors correlate well, one sensor can be used to predict the response of another. Of particular interest is predicting ice albedo, which appears possible for bare ice. Snow cover, however, affects albedo more strongly than the other sensors, and it appears to be anticorrelated in some cases; thus, it is difficult for microwave sensors to predict albedo. This implies, however, that microwave and visible/infrared sensing used together should be useful in predicting the existence as well as some properties of the snow.

Theoretical models for the visible, infrared, and microwave regions have produced agreement for a number of cases. They show that it is necessary to consider the vertical structural variations in the ice and snow to produce a consistent picture over the broad range of wavelengths and active/passive sensors available here. The results for the visible and near infrared show that the ice and snow were not pure and that the effects of particulates, dissolved material, and soot were significant. The direct effects of these embedded substances at infrared and microwave frequencies should be negligible because they would not perturb the bulk dielectric properties of the ice or snow and the size of the particles were too small to scatter significant amounts of radiation. Indirect effects are possible where the embedded material could alter the brine volume through chemical reactions or through enhancement of the solar heating. For the present cases, however, these effects are assumed to be negligible.

PCA has proved useful in analyzing the multidimensional structure data set and makes it possible to suggest multisensor combinations that should improve the ability to resolve ice type via remote sensing. The present conclusion are based on near-surface measurements do not take into account the influence of cloud cover and other environmental factors that limit the ability to observe the surface via remote sensing.

In cases in which direct comparisons have been made between field and pond observations, the structure and EM signatures of corresponding ice types in the field and those grown at the GRF pond facility are essentially the same. Salinity and density profiles are very similar, and the air temperature regimes cover the same range (-5 to -30 °C). In cases in which differences in EM signatures are observed, they can be explained via the models as resulting from well-understood physics principles, such as differences in ice thickness, snow thickness, or penetration depth. We conclude that the information gained during the pond experiments can be compared in a meaningful and useful way with the field results to study the signature behavior of new and young ice types.

References

[1] G. A. Maykut, "Large scale heat exchange and ice production in the central Arctic," *J. Geophys. Res.*, vol. 87, pp. 7971–7984, 1982.

[2] T. C. Grenfell, D. J. Cavalieri, J. C. Comiso, M. R. Drinkwater, R. G. Onstott, I. Rubinstein, K. Steffen, and D. P. Winebrenner, "Considerations for remote sensing of thin sea ice," *Microwave Remote Sensing of Sea Ice*, F. Carsey, Ed. Washington, DC: Amer. Geophys. Union, 1992, pp. 291–300.

[3] D. T. Eppler, M. R. Anderson, D. J. Cavalieri, J. Comiso, L. D. Farmer, C. Garrity, P. Gloersen, T. C. Grenfell, M. Hallikainen, A. W. Lohanick, C. Maetzler, R. A. Melloh, I. Rubinstein, and C. T. Swift, "Passive microwave signatures of sea ice," *Microwave Remote Sensing of Sea Ice*, F. Carsey, Ed. Washington, DC: Amer. Geophys. Union, 1992, pp. 47–68.

[4] R. G. Onstott, "SAR and scatterometer signatures of sea ice," *Microwave Remote Sensing of Sea Ice*, F. Carsey, Ed. Washington, DC: Amer. Geophys. Union, 1992, p. 73.

[5] T. C. Grenfell, "Microwave and thermal infrared emission from young sea ice and pancake ice," in *Proc. IGARSS'96*, pp. 1199–1201.

[6] S. V. Nghiem, R. Kwok, S. H. Yueh, and M. R. Drinkwater, "Polarimetric signatures of sea ice, 2, experimental observations," *J. Geophys. Res.*, vol. 100, no. C7, pp. 13 681–13 698, 1995.

[7] ——, "Polarimetric signatures of sea ice, 1, theoretical model," *J. Geophys. Res.*, vol. 100, no. C7, pp. 13 665–13 679, 1995.

[8] S. V. Nghiem, R. Kwok, J. A. Kong, R. T. Shin, S. A. Arcone, and A. J. Gow, "An electrothermodynamic model with distributed properties for effective permittivities of sea ice," *Radio Sci.*, vol. 31, no. 2, pp. 297–311, 1996.

[9] S. V. Nghiem, R. Kwok, S. H. Yueh, A. J. Gow, D. K. Perovich, J. A. Kong, and C.-C. Hsu, "Evolution in polarimetric signatures of thin saline ice under constant growth," *Radio Sci.*, vol. 32, no. 1, pp. 127–151, 1997.

[10] S. V. Nghiem, S. Martin, D. K. Perovich, R. Kwok, R. Drucker, and A. J. Gow, "A laboratory study of the effects of frost flowers on C-band radar backscatter from sea ice," *J. Geophys. Res.*, vol. 102, no. C2, pp. 3357–3370, 1997.

[11] W. B. Tucker, III, T. C. Grenfell, R. G. Onstott, D. K. Perovich, A. J. Gow, R. A. Shuchman, and L. L. Sutherland, "Microwave and physical properties of sea ice in the winter marginal ice zone," *J. Geophys. Res.*, vol. 96, pp. 4573–4587, 1991.

[12] Jezek *et al.*, "Electromagnetic properties of sea ice," ARI Rev. Paper, 1998.

[13] D. K. Perovich and A. J. Gow, "A quantitative description of sea ice inclusions," *J. Geophys. Res.*, vol. 101, no. 18, pp. 327–343, 1996.

[14] C. T. Swift, K. St. Germain, K. C. Jezek, S. P. Gogineni, A. J. Gow, D. K. Perovich, T. C. Grenfell, and R. G. Onstott, "Laboratory investigations of the electro-magnetic properties of artificial sea ice," *Microwave Remote Sensing of Sea Ice*, F. Carsey, Ed. Washington, DC: Amer. Geophys. Union, 1992, pp. 177–199.

[15] T. C. Grenfell, M. R. Wensnahan, and D. P. Winebrenner, "Passive microwave and infrared observations of new and young sea ice—The 1994 CRREL pond experiment," in *Proc. PIERS Symp.*, 1995, p. 66.
[16] T. C. Grenfell, D. P. Winebrenner, and A. W. Lohanick, "Passive microwave and thermal infrared emissivities of first-year sea ice near Point Barrow Alaska," in *Proc. PIERS Symp.*, 1995, p. 479.
[17] S. V. Nghiem, R. Kwok, S. H. Yueh, D. K. Perovich, A. J. Gow, C.-C. Hsu, K.-H. Ding, J. A. Kong, and T. C. Grenfell, "Diurnal thermal cycling effects on microwave signatures of thin sea ice," *IEEE Trans. Geosci. Remote Sensing*, vol. 36, pp. 111–124, Jan. 1998.
[18] J. Dozier and S. G. Warren, "Effects of viewing angle on the infrared brightness temperature of snow," *Water Resourc. Res.*, vol. 18, no. 5, pp. 1424–1434, 1982.
[19] J. W. Salisbury, D. M. D'Aria, and A. Wald, "Measurements of thermal infrared spectral reflectance of frost, snow, and ice," *J. Geophys. Res.*, vol. 99, no. B12, pp. 24 235–24 240, 1994.
[20] C. S. Roesler and R. Iturriaga, "Absorption properties of marine-derived material in Arctic sea ice," in *Proc. SPIE Ocean Opt. XII*, 1994, vol. 2258, pp. 933–943.
[21] T. C. Grenfell and D. K. Perovich, "Radiation absorption coefficients of polycrystalline ice from 400–1000 nm," *J. Geophys. Res.*, vol. 86, pp. 7447–7450, 1981.
[22] D. K. Perovich and J. W. Govoni, "Absorption coefficients of ice from 250 to 400 nm," *J. Geophys. Res. Lett.*, vol. 19, pp. 1233–1235, 1991.
[23] C. D. Mobley, G. F. Cota, T. C. Grenfell, R. A. Maffione, W. S. Pegau, and D. K. Perovich, "Modeling light propagation in sea ice," this issue, pp. 1743–1749.
[24] K. M. Golden, M. Cheney, A. K. Fung, T. C. Grenfell, D. Isaacson, J. A. Kong, S. V. Nghiem, J. Sylvester, and D. P. Winebrenner, "Forward electromagnetic scattering models for sea ice," this issue, pp. 1655–1674.
[25] D. K. Perovich, J. Longacre, D. G. Barber, R. A. Maffione, G. F. Cota, C. D. Mobley, A. J. Gow, R. G Onstott, T. C. Grenfell, W. S. Pegau, M. Landry, and C. S. Roesler, "Field observations of the electromagnetic properties of first-year sea ice," this issue, pp. 1705–1715.
[26] M. R. Wensnahan, "Evolution of the passive microwave signature of thin sea ice," Ph.D. dissertation, Univ. Washington, 1995.
[27] T. C. Grenfell, S. G. Warren, and P. C. Mullen, "Reflection of solar radiation by the Antarctic snow surface at ultraviolet, visible, and near-infrared wavelengths," *J. Geophys. Res.*, vol. 99(D9), no. 18, pp. 669–684, 1994.
[28] T. C. Grenfell, "A radiative transfer model for sea ice with vertical structure variations," *J. Geophs. Res.*, vol. 96, no. C9, pp. 16 991–17 001, 1991.
[29] D. K. Perovich, personal communication, 1996.
[30] S. G. Warren and W. J. Wiscombe, "A model for the spectral albedo of snow—II: Snow containing atmospheric aerosols," *J. Atmos. Sci.*, vol. 37, no. 12, pp. 2734–2745, 1980.
[31] R. G. Onstott, P. Gogenini, A. J. Gow, T. C. Grenfell, K. C. Jezek, D. K. Perovich, and C. T. Swift, "Electromagnetic and physical properties of sea ice formed in the presence of wave action," this issue, pp. 1764–1783.
[32] T. C. Grenfell, D. L. Bell, A. W. Lohanick, C. T. Swift, and K. St. Germain, "Multifrequency passive microwave observations of saline ice grown in a tank," in *Proc. IGARSS'88*, pp. 1687–1690.
[33] D. K. Perovich, C. S. Roesler, and W. S. Pegau, "Variability in optical properties of Arctic sea ice," *J. Geophys. Res.*, to be published.
[34] A. W. Lohanick and T. C. Grenfell, "Variations in brightness temperature over cold first-year sea ice near Tuktoyaktuk, Northwest Territories," *J. Geophys. Res.*, vol. 91, no. C4, pp. 5133–5144, 1986.
[35] D. G. Barber, A. K. Fung, T. C. Grenfell, S. V. Nghiem, R. G Onstott, V. I. Lytle, D. K. Perovich, and A. J. Gow, "The role of snow on microwave emission and scattering over first-year sea ice," this issue, pp. 1750–1763.
[36] K. M. St. Germain, C. T. Swift, and T. C. Grenfell, "Determination of dielectric constant of young sea ice using microwave spectral radiometry," *J. Geophys. Res.*, vol. 98, no. C3, pp. 4675–4697, 1993.
[37] M. Wensnahan, G. A. Maykut, and T. C. Grenfell, "Passive microwave remote sensing of thin sea ice using principal component analysis," *J. Geophys. Res.*, vol. 98, no. C7, pp. 12 453–12 468, 1993.
[38] T. C. Grenfell, personal communication.

Thomas C. Grenfell (M'94–A'95), for a photograph and biography, see p. 124 of the January 1998 issue of this TRANSACTIONS.

David G. Barber, for a photograph and biography, see p. 50 of the January 1998 issue of this TRANSACTIONS.

A. K. Fung (S'60–M'66–SM'70–F'85), photograph and biography not available at the time of publication.

Anthony J. Gow, for a photograph and biography, see p. 124 of the January 1998 issue of this TRANSACTIONS.

Kenneth C. Jezek (A'92), photograph and biography not available at the time of publication.

E. J. Knapp, photograph and biography not available at the time of publication.

Son V. Nghiem (M'86), for a photograph and biography, see p. 123 of the January 1998 issue of this TRANSACTIONS.

Robert G. Onstott (S'73–M'79), photograph and biography not available at the time of publication.

Donald K. Perovich, for a photograph and biography, see p. 124 of the January 1998 issue of this TRANSACTIONS.

Collin S. Roesler, photograph and biography not available at the time of publication.

C. T. Swift (M'67–SM'69–F'83), photograph and biography not available at the time of publication.

F. Tanis, photograph and biography not available at the time of publication.